Pergamon

PII: S0967-0637(97)00024-1

Deep-Sea Research I, Vol. 44, No. 8, pp. 1427–1450, 1997

0967-0637/97 $17.00 + 0.00

Eddy-induced nutrient supply and new production in the Sargasso Sea

D. J. McGILLICUDDY, JR* and A. R. ROBINSON†

(*Received* 2 *August* 1996; *in revised form* 21 *January* 1997; *accepted* 7 *February* 1997)

Abstract—A limited area, eddy resolving coupled physical and biological model is used to examine the role of mesoscale dynamical processes in nutrient cycling in the Sargasso Sea. Upwelling due to the formation of cyclonic eddies and their intensification caused by interaction with surrounding mesoscale features causes spatially and temporally intermittent fluxes of nitrate into the euphotic zone. The annual flux resulting from this eddy upwelling process is of the order of 0.5 mol N m^{-2} $year^{-1}$, which is sufficient to sustain a rate of new primary production that is consistent with estimates for this region derived from budgets of oxygen and other dissolved gases.

INTRODUCTION

In the oligotrophic waters of the open ocean, the availability of nitrogenous nutrients limits phytoplankton production throughout most of the year. With the exception of the late wintertime period, during which wind and convectively driven vertical mixing punctures the nutricline, surface waters are generally nutrient depleted. In traditional paradigms of open ocean plankton ecology (Dugdale and Goering, 1967; Eppley and Peterson, 1979), the predominant source of phytoplankton nutrition in these relatively unproductive water masses is thought to be the byproducts of secondary production (primarily ammonia and urea) commonly referred to in aggregate as recycled nutrients. In such a scenario, only a small portion of the total primary production is fueled by exogenous nitrogen (mostly nitrate) transported into the euphotic zone from the deep sea. This "new" production is a cornerstone of oceanic biogeochemical cycling in that it provides a fundamental constraint on the amount of biologically fixed material that is exported to the deep sea.

The conventional views of oligotrophic ecosystems have been called into question by a variety of inferences made from observations of transient tracer distributions. The rate of primary production implied by the seasonal subsurface accumulation of oxygen in the euphotic zone (which by definition is linked to new rather than total production) is large relative to the total production as measured from carbon uptake in incubation experiments (Shulenberger and Reid, 1981; Jenkins and Goldman, 1985). Subsequent investigations comparing these changes in dissolved oxygen inventories with those of argon have confirmed the observed signal to be of predominantly biological origin (Craig and Hayward, 1987; Spitzer and Jenkins, 1989). Careful quantitative analysis of the uncertainties involved in such oxygen budget calculations has been carried out using

* Department of Applied Ocean Physics and Engineering, Woods Hole Oceanographic Institution, Woods Hole, MA 02543, U.S.A.

† Department of Earth and Planetary Sciences, Harvard University, Cambridge, MA 02138 U.S.A.

realistic one dimensional physical models of the upper ocean with coupled gas dynamics, which essentially confirm the prior estimates (Musgrave *et al.*, 1988; Spitzer and Jenkins, 1989). New production estimates based on oxygen consumption below the euphotic zone are also at odds with the traditional view. Deep sea oxygen utilization rates computed from apparent oxygen utilization estimates and water mass age derived from both the $^{3}H/^{3}He$ clock (Jenkins, 1982; Jenkins and Goldman, 1985) and the $^{3}H/^{228}Ra$ clock (Sarmiento *et al.*, 1993) are consistent with the decay of an export flux commensurate to that which produced the overlying oxygen accumulation. Evidence of the upward flux of nutrients required to sustain this level of new production was introduced by Jenkins (1988a). Using the measured excess ^{3}He dissolved in the mixed layer together with estimated rates of outgassing to the atmosphere, he inferred the rate of supply of deep sea tritiugenic helium to the surface waters under an assumption of steady state. Combining this with the observed ^{3}He–NO_3 correlation below the euphotic zone yields a vertical nitrate flux capable of supporting the amount of new production implied by the oxygen budgets.

Several different lines of evidence have thus indicated an estimate of new primary production that conflicts with that based on measured total productivity and traditional views that only a small portion of that total is supported by new nitrogen. Some have argued this implies methodological problems with ^{14}C incubations that cause substantial underestimation of total production (Shulenberger and Reid, 1981; Jenkins and Goldman, 1985), while others have challenged the assumptions that the *f*-ratio is constant and low (Platt and Harrison, 1985).

A major complication involved in reconciling these biogeochemical budgets lies in the fact that the tracer observations reveal integral balances on time and space scales not sampled by discrete bottle incubation experiments. The potential incompatibility of explicitly resolved scales in these two types of measurement raises at least two possible explanations for the apparent discrepancy. First, the biogeochemical budgets could be inherently three-dimensional. Rintoul and Wunsch (1990) argued this point on the basis of a large scale nutrient flux divergence computed from basin-wide zonal sections at 26°N and 34°N. Speculating that the net flux of nitrate out of the region is balanced by an input of dissolved organic nitrogen, they infer that a substantial fraction of the apparent oxygen utilization in the deep ocean is a result of remineralization of organic matter fixed elsewhere (presumably somewhere north of 34°N) and subsequently advected into the region. While this could explain how, at a particular location in the Sargasso Sea, oxygen consumption at depth could exceed oxygen production in the euphotic zone, it does not account for the high oxygen production in the near surface waters.

A second possibility is that traditional time series sampling underresolves intermittent events that have a disproportionately large impact on the overall budgets. It has been hypothesized that sporadic bursts of diapycnal mixing could cause large fluxes of nitrate into the euphotic zone (Jenkins and Goldman, 1985, vis-à-vis Klein and Coste, 1984), but mixing rates inferred from microstructure measurements do not support this claim (Lewis *et al.*, 1986). The possibility that mesoscale eddies could play a role in nutrient supply to the upper ocean has been suggested by several authors (Angel and Fasham, 1983; Franks *et al.*, 1986; Woods, 1988; Falkowski *et al.*, 1991; Strass, 1992; Onken, 1992; Flierl and Davis, 1993; McGillicuddy *et al.*, 1995a). Jenkins (1988b) documents some provocative observations of an anomalous water mass near Bermuda in the summer of 1986 showing excess ^{3}He and nitrate in the upper ocean that could have arisen only from a recent injection of water from the deep sea. His calculations indicate that only a few such events each year

could fuel the level of new production indicated by the tracer observations. Unfortunately, the current observational database is not sufficient to provide detailed study of the dynamics of such events, not to mention quantitative assessment of their impact on the overall budgets. The spatial and temporal intermittency of these processes poses a difficult sampling problem: proper resolution requires a time series of synoptic three-dimensional physical and biogeochemical measurements conducted at the right place at the right time.

Although the dynamics and statistics of such processes are inaccessible through observations alone, the combination of available measurements with realistic numerical models of ocean circulation offers a context in which this issue can be addressed. In this study, a very simple "nutrient model" is incorporated into a limited area eddy resolving model of the open ocean. Coupled three-dimensional simulations are used to examine the nature of mesoscale dynamical events that induce nitrate flux into the euphotic zone through vertical displacements of the density (and therefore nutrient) surfaces. Spatial and temporal averages of the simulated fields are then used to estimate the integrated annual nitrate flux associated with these intermittent events.

METHODS

The general vertical structure of the open ocean nutrient field is composed of an oligotrophic near surface region where nutrients have been depleted by photosynthetic activity and the underlying thermocline waters rich in nutrients due to the decay of sinking organic material. These counterbalancing biological processes result in a tight correlation between nitrate and density in the portion of the water column below the euphotic zone. This relationship forms the basis for the influence of oceanic eddies on upper ocean nutrient cycling. Vertical displacements of the main thermocline associated with mesoscale features deliver nitrate into the euphotic zone in the case of upwelling and remove nutrient depleted water in the downwelling case. Light imposes a fundamental asymmetry in this system, causing upwelled nutrients to be fixed into organic material thereby rectifying vertical transports of both signs into a net upward flux. This upward transport of nutrients is balanced by a downward flux of sinking organic material from which nutrients are remineralized during the processes associated with its decay.

The approach used here to study this process is to incorporate a simple nutrient transport model into a realistic model of the mid-ocean eddy field. The essential physics of mid-ocean mesoscale eddies is captured by quasigeostrophy. Relevance of the QG equations to this type of motion has been established on theoretical grounds (Bretherton and Karweit, 1975; Charney and Flierl, 1981), analysis of observations (McWilliams, 1976), numerical simulation (Haidvogel, 1983), ocean prediction experiments (Robinson and Leslie, 1985; Carton, 1986; Walstad and Robinson, 1990), and detailed analysis of physical processes associated with the dynamics of these flows (Pinardi and Robinson, 1987; Spall, 1989). Resolution requirements imposed by the space and time scales of interest necessitate the use of a limited area model. An open boundary QG model (Robinson and Walstad, 1987) with a coupled surface boundary layer (Walstad and Robinson, 1993) was thus chosen as a basis for the work described herein. This model has been calibrated for use in interdisciplinary problems (McGillicuddy, 1993; McGillicuddy and Robinson, in press) and used extensively for coupled physical biological interactions in the northeast Atlantic (McGillicuddy *et al.*, 1995a,b). Details of the models are summarized in Appendix 1.

The experimental design is to force the model along the boundaries of a large (1000 km^2)

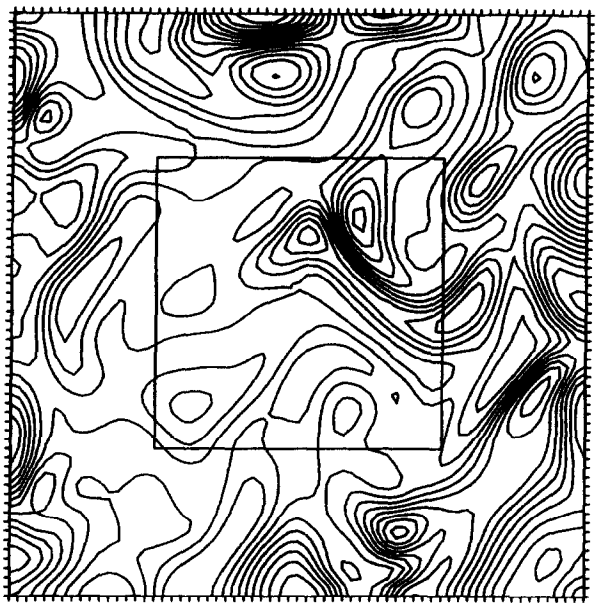

Fig. 1. Simulated sea surface temperature field after 880 days of integration. The entire model domain is 1000 km on a side, and the dimensions of the interior subdomain from which simulated data are extracted are 500 km by 500 km. Contour interval is 0.2°C.

domain with time-dependent statistical representations of typical synoptic features in the region. This boundary forcing consists of Rossby wave fits to the MODE data computed by McWilliams and Flierl (1976), including the surface intensification of modal amplitudes documented by McWilliams (1974). The surface boundary layer is forced with the climatological mean summertime wind of 5.1 m s^{-1} and zero net heat flux. The mixed layer is specified to be constant at a depth of 25 m. Starting from an arbitrary initial condition, the model is run out to statistical steady state. Far enough away from the direct boundary forcing, the freely evolving interior takes on a realistic character (Fig. 1). Simulated fields are therefore extracted from an interior 500 km^2 subdomain for analysis. This technique has been used to produce environmental fields for forecasting studies in the region by Robinson and Haidvogel (1980) and Miller and Robinson (1984). This configuration was deliberately chosen over other alternatives (such as spin-down in a doubly periodic domain) to facilitate long-term simulations from which robust statistics can be derived.

The nutrient transport model is based on the nitrate–density relationship derived from the Joint Global Ocean Flux Study's Bermuda Atlantic Time Series Station (BATS) (Fig. 2). These data can be conveniently grouped into three categories that are amenable to a piecewise linear fit. In waters denser than $\sigma_T = 26.2$, a roughly linear relationship exists. Nitrate is generally depleted in fluid more buoyant than $\sigma_T = 25.8$, although some noticeable departures do occur. Considerable scatter exists in the interval between these two cut-off values, which is most likely associated with seasonal mixing events. Because the objective of the present study is to focus on mesoscale processes, which we hypothesize dominate nutrient supply during most of the year excepting wintertime periods of convective mixing

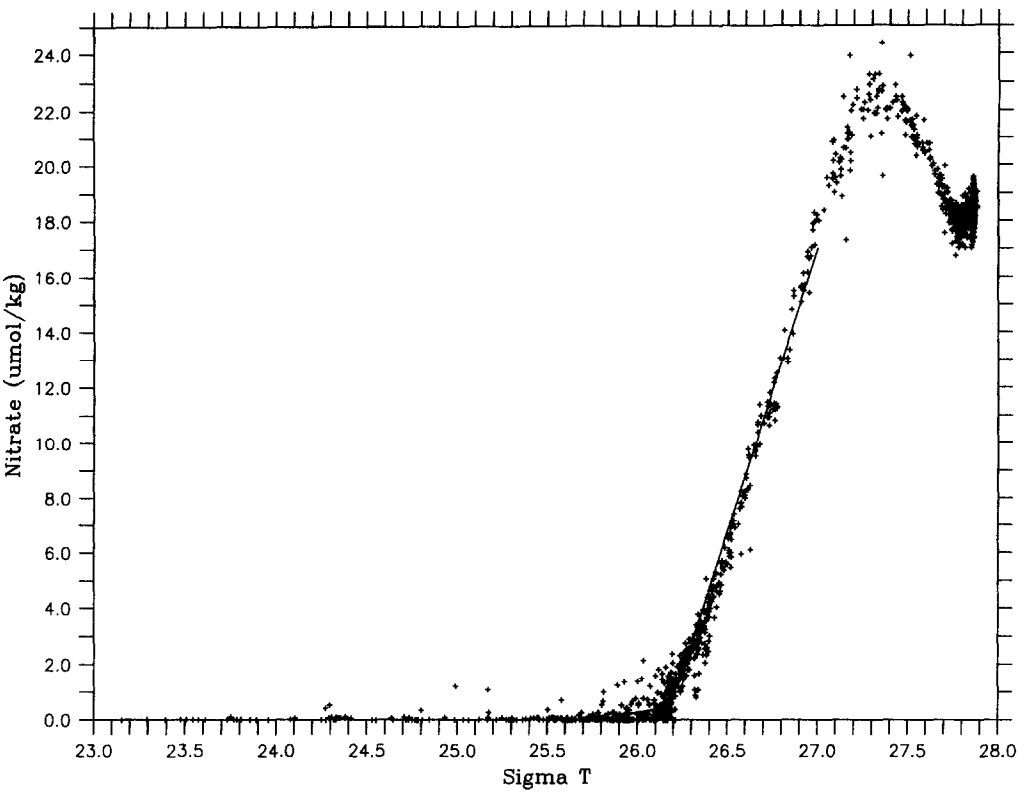

Fig. 2. Nitrate plotted as a function of sigma T for all observations during the first four years of the BATS time series. The solid line indicates the piecewise linear fit to the data used in the nutrient transport model.

(see below), the higher nitrate values in this interval are excluded from the fit. This results in a nitrate–σ_T relationship that can be articulated as

$$\overline{NO_3} = 0 \qquad \sigma_T < 25.8$$

$$\overline{NO_3} = 1.27(\sigma_T - 25.8) \qquad 25.8 \leq \sigma_T < 26.2$$

$$\overline{NO_3} = .5 + 20.5(\sigma_T - 26.2) \qquad \sigma_T > 26.2$$

This relationship is specified at the boundaries so that fluid coming into the domain has the appropriate nutrient properties. The "dynamics" of the nutrient transport model are formulated as complete removal of all nitrate in the euphotic zone (EZ) every time step (Δt) and relaxation to the observed $NO_3(\sigma_T)$ relationship below:

$$\frac{\partial NO_3}{\partial t} = -\frac{NO_3}{\Delta t} \qquad z \geq z_{EZ}$$

$$\frac{\partial NO_3}{\partial t} = R(\overline{NO_3}(\sigma_T(x, y, z, t)) - NO_3) \qquad z < z_{EZ}$$

In this context the euphotic zone is defined as the depth interval over which nitrate is completely utilized. Observed summertime mean nitrate concentrations at BATS drop

below the limit of detection at approximately 75 m, which is well below the mixed layer during this highly stratified period. Clearly, some nitrate uptake does occur below this depth horizon, as the traditionally defined euphotic zone (the depth at which irradiance is one percent of its surface value) is some 25 m deeper than the z_{EZ} chosen here. Therefore in this respect the present model parameterizes biological utilization conservatively by prescribing $z_{EZ}=75$ m. While this simplistic model is a crude approximation to the complex biological processes occurring in the Sargasso Sea, it provides a straightforward accounting method for keeping track of the simulated fluxes of nitrogen induced by the eddies. Future work will address the ramifications of more sophisticated physiological and ecological formulations.

The underlying assumptions of the nutrient transport model are: (1) nitrate is utilized on faster times scales than the duration of intermittent bursts of supply, and (2) the $NO_3(\sigma T)$ relationship is restored below the euphotic zone on time scales comparable to or shorter than the period of the vertical displacements associated with the supply events. The former can be justified on several different grounds. Nutrient enrichment incubation experiments document ample uptake capacity of the phytoplankton community. With doubling times on the order of one day, the population response time is quite rapid with respect to the physical forcing. Finally, near surface nitrate concentrations hardly ever exceed the limit of detection except during strong winter mixing events.

The latter assumption is more subtle. Consider a fluid parcel caught in an upwelling event. As the parcel rises in the water column, nitrate is removed. As the parcel is subsequently downwelled into the aphotic zone, it is refortified with nitrate that is remineralized during processes that occur in association with the decay of sinking particulate material. Thus, it will bring new nitrate with it the next time it is upwelled. If the period of the vertical displacements were fast compared to this restoring time scale, such a model would tend to overpredict the upward flux of new nitrate. However, such does not appear to be the case. The results described in the following sections will show that the relevant time scale of nutrient injections associated with mesoscale dynamics is that of an eddy lifetime. Typical eddy lifetimes in these simulations are of the order of half a year, which is consistent with Lagrangian drifter observations in the region, which document persistence of individual features for periods up to 430 days (see review by Richardson, 1993). Given that an upwelled fluid parcel will be, statistically speaking, downwelled in the next dynamical event in which it participates, it can be argued that the nominal period of vertical displacements is on the order of a year. An estimate of the remineralization time scale associated with the hypothesized eddy injection events can be computed using typical nitracline displacements (90 m) and sinking rates of particulate material (1 m day^{-1}). These characteristics imply a restoring time scale of approximately 3 months ($R=0.01\ d^{-1}$), which is considerably shorter than that associated with the pertinent eddy fluctuations. Numerical experiments confirm that the results described below are relatively insensitive to the parameter R.

RESULTS

Time series of enstrophy (mean square vorticity) and kinetic energy integrated over the subdomain (Fig. 3) show that the interior fields reach a statistical steady state after about 400 days of integration.* The following analysis of the fields is therefore based on the final

*Additional simulations (not shown) run out for a period of 8 years confirm the stability of this steady state.

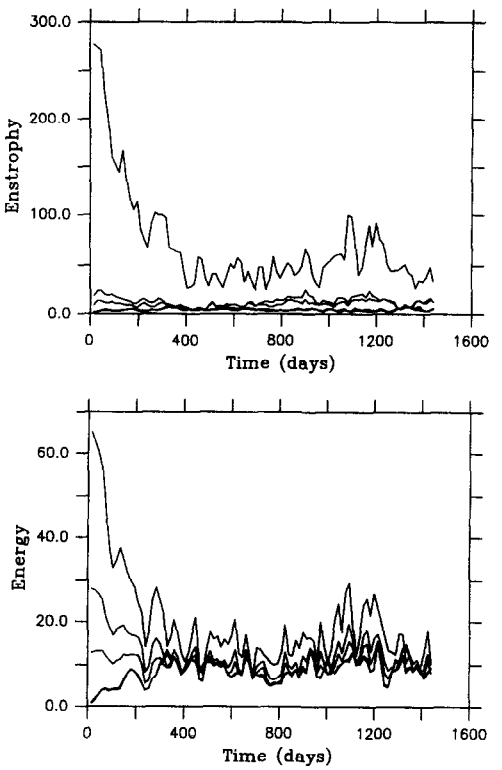

Fig. 3. Time series of nondimensional enstrophy (mean square vorticity) and kinetic energy at six model levels integrated over the interior subdomain indicated in Fig. 1.

2 years of the 4-year calculation, well after the initial adjustment period. Kinetic energy spectra computed from the simulation are consistent with those derived from moored current meter measurements (Fig. 4) on the time scales of mesoscale eddy evolution (weeks to months). Of course a regional model of this type cannot properly represent lower frequency phenomena, which are most likely associated with the larger scale circulation, or higher frequency phenomena, whose physics is not represented in the model equations and which occur on scales smaller than the computational grid. However, for the frequencies of interest here, the energy content of the simulated fields is mostly consistent with observations, with a few obvious exceptions (e.g. 400 m meridional is somewhat low; 1400 and 3950 m zonal are too high). The dominant spatial scales in the model solution also agree with data. Figure 5 shows that the 600 m model temperature autocorrelation function is quite similar in structure to that computed from MODE hydrographic measurements at 515 m. Thus, from a statistical point of view, it appears that this simulation is a realistic representation of the eddies that predominate thermocline fluctuations in the ocean's interior in the Sargasso Sea.

A typical time series of synoptic fields extracted from this simulation is shown in Fig. 6. On day 850 a pair of warm and cold eddies are present in the northeast corner of the domain. Ten days later, the eddies are strongly interacting, with a tail of the warm eddy wrapping south around the western flank of the cold eddy. Both features have intensified during the

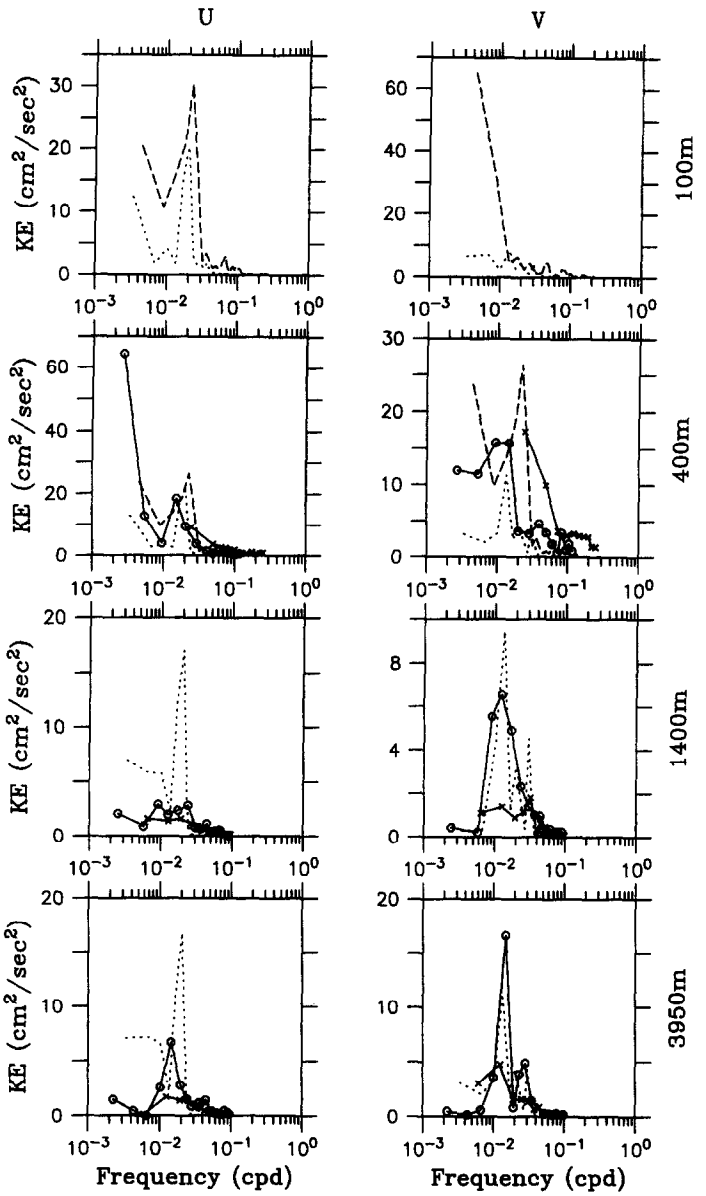

Fig. 4. Comparison of zonal and meridional kinetic energy spectra at various depths computed in the interior subdomain during the final two years of the simulation (dotted lines) with those computed from moored current meter measurements (dashed line: POLYMODE central mooring at 269 m and 394 m; circles: MODE center at 500 m, 1500 m and 4000 m; crosses: MODE east at 500 m, 1500 m and 4000 m. MODE spectra digitized from Richman *et al.* (1977)).

interaction. Between days 860 and 870, the tail of the warm eddy has snapped off, leaving a visible remnant of it south-west of its original position. The cold eddy has been stretched into an elongate form running east–west. On day 880, the cold feature begins to split into two smaller parts. This process is completed by day 890, when the warm feature has

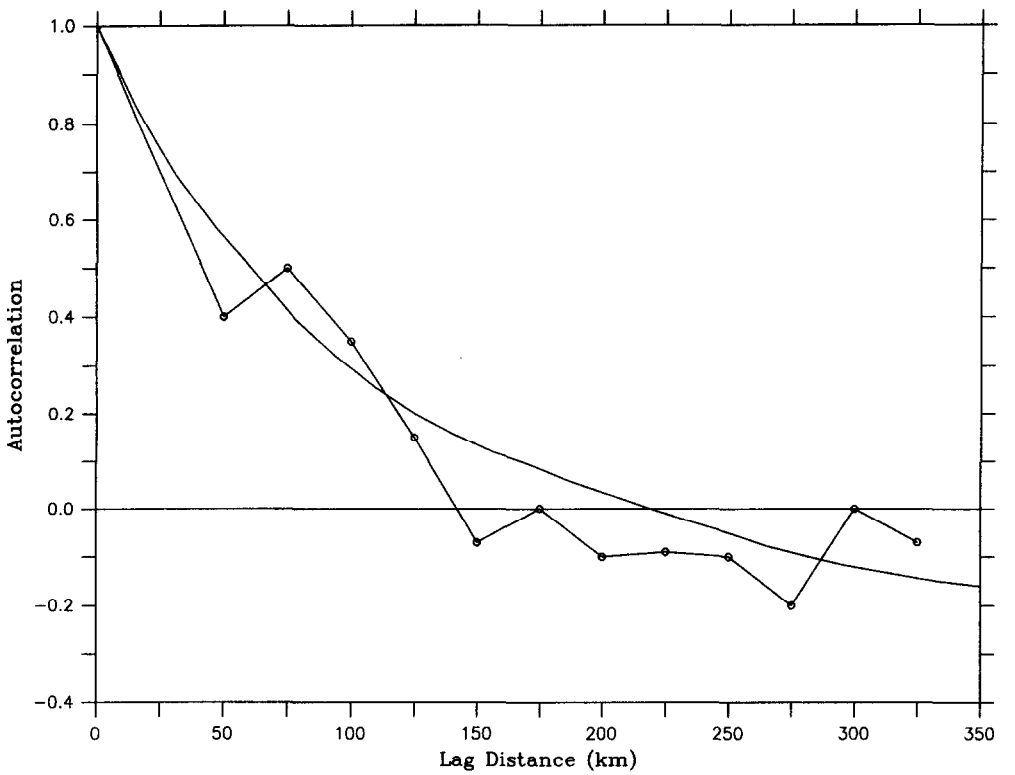

Fig. 5. Comparison of the 600 m model temperature autocorrelation function computed in the interior subdomain during the final 2 years of the simulation (solid line) with that computed at 515 m from MODE hydrography (circles).

elongated into a north–south oriented lunate form. The offspring of the original cold feature reside to the west and south-east of the warm eddy, with the latter of the two mostly outside the domain. A third cold eddy enters the domain between days 880 and 890 and is swept south-westward into the concave portion of the warm feature by day 900.

The nutrient fluxes associated with these dynamical events are shown in Fig. 7. Little activity is present on day 850, as the eddy field is relatively quiescent. Shortly thereafter, a burst of nitrate flux occurs as the cold eddy intensifies during its interaction with the warm eddy. Initially domed density surfaces inside the cold eddy have been forced upward even further as a result of this energetic interaction, causing a strong pulse of nitrate flux in the interior of the feature, clearly evident on day 860. As the cold eddy is subsequently stretched east–west, weaker nitrate flux is apparent along its northern and southern borders (day 870). The next major upwelling event occurs with the breakup of the elongated cold feature. Significant injections of nitrate result from upwelling inside the newly formed features (day 880). As the south-eastern cold feature drifts out of view, the nitrate flux associated with its sibling continues (days 890–900). Also evident during this time period is the patch of nitrate enhancement brought about by the interaction of the third cold feature and the warm eddy.

The time series of integrated nitrate flux spatially averaged over the 500 km^2 subdomain is shown in Fig. 8 (solid line). After a period of anomalously high nitrate flux associated with the adjustment to initial conditions, the rate of increase in the total amount of nitrate transported into the euphotic zone is relatively constant. The slope of the linear least squares fit to this line can thus be used to estimate the spatially averaged upward flux. This amounts to a net flux of 0.5 mol N m^{-2} year^{-1} into the euphotic zone. For comparison purposes a twin numerical experiment was conducted in the absence of wind forcing (dashed line, Fig. 8). The nitrate flux computed from the least squares fit to the "no wind" case is 0.36 mol N m^{-2} year^{-1}, or about 72% of the central simulation.

DISCUSSION

Vertical motions in the open ocean arise from a variety of processes associated with both the thermohaline and wind-driven circulation. The former category is composed of an overturning cell that is convectively driven by deep water formation in limited areas. This vigorous localized sinking is thought to be balanced by very gentle large scale upwelling, which is so sluggish that it is an essentially irrelevant nutrient supply on time scales shorter than many hundreds of years. Spatial variations in wind forcing (i.e. wind stress curl) induce vertical motion by creating convergences and divergences in the wind driven surface current. Large scale wind patterns over the main subtropical gyres generally result in a net surface convergence, thus inducing downwelling in these regions. Typical downwelling rates associated with this process in the Sargasso Sea are on the order of 0.1 m day^{-1} (Leetma and Bunker, 1978). Wind stress curl driven downwelling in this region is greatly overshadowed by vertical motions of two other types, which are at least an order of magnitude greater. Vortex stretching associated with quasigeostrophic dynamics of mesoscale eddies produces patches of vertical velocity of the order of one to several meters per day with horizontal scales ranging from the submesoscale (order 10 km) up to the scale of the eddies themselves (order 100 km). In addition to these vertical motions, which occur in the absence of direct wind forcing, vertical transports are also induced by the interaction of these interior flows with the surface Ekman drift. The superposition of the wind-driven surface current on the mesoscale eddy velocity field creates patches of convergence and divergence that must be balanced by vertical transport. Stated differently, advection of the interior vorticity field by the surface current induces vortex stretching in the near surface layer. This type of vertical motion has been characterized as an additional term in the generalized Ekman divergence (Niiler, 1969; Lee *et al.*, 1994).

The results described in the previous section demonstrate that the dominant mechanism of nitrate transport associated with mesoscale eddies arises from their internal dynamics. Comparison of wind forced versus non-wind forced simulations shows that only about 30% of the total nitrate flux arises from the vertical transport induced by the interaction of the surface current with the interior flow. Analysis of the synoptic patterns of simulated nitrate flux such as those shown in Fig. 7 reveals that the most prevalent nutrient injections occur in the interiors of cyclonic eddies during their formation and intermittent intensification resulting from interaction with other mesoscale features. A conceptual model of this process is illustrated in Fig. 9. Consider a density surface with mean depth Z_0 which is coincident with the depth of the euphotic zone. This density surface is perturbed about its mean depth by the formation, evolution and destruction of mesoscale features. Intensifying warm eddies move the surface down, while cold eddies raise it toward the surface. Nutrients injected into

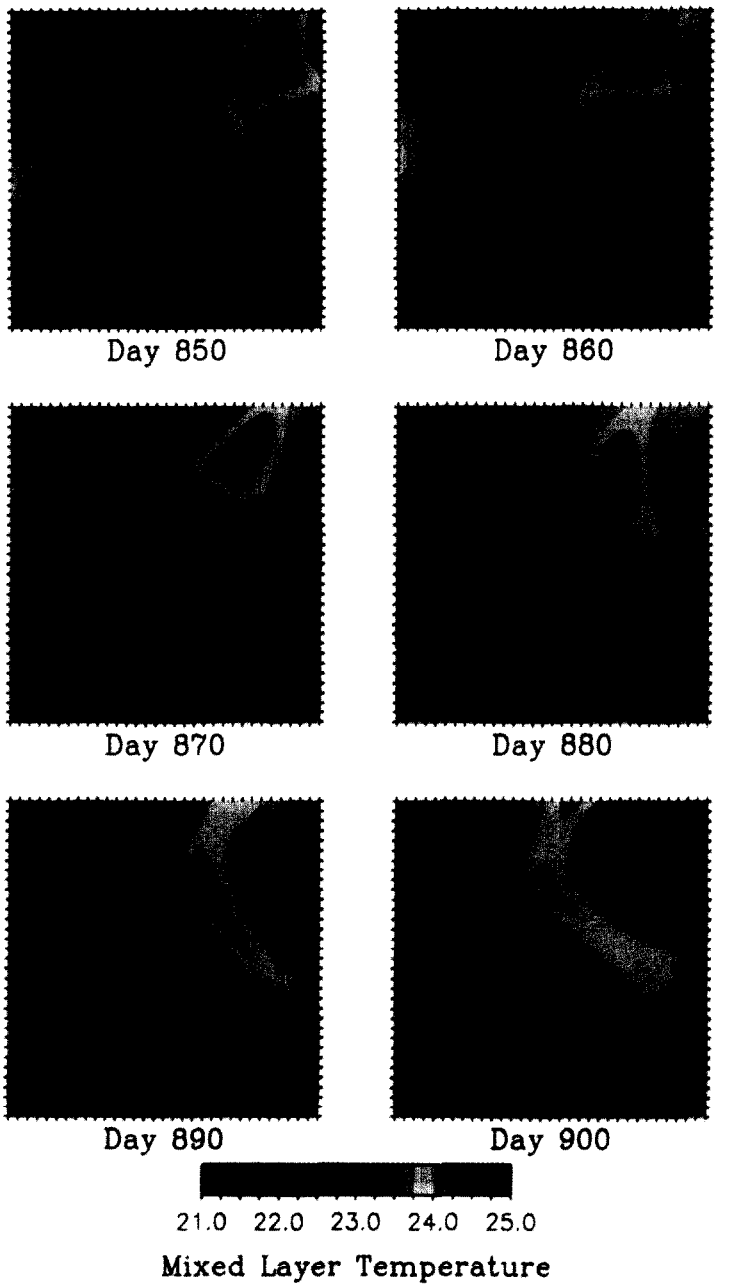

Fig. 6. Time series of simulated mixed layer temperature fields (°C) extracted from the interior subdomain during days 850–900.

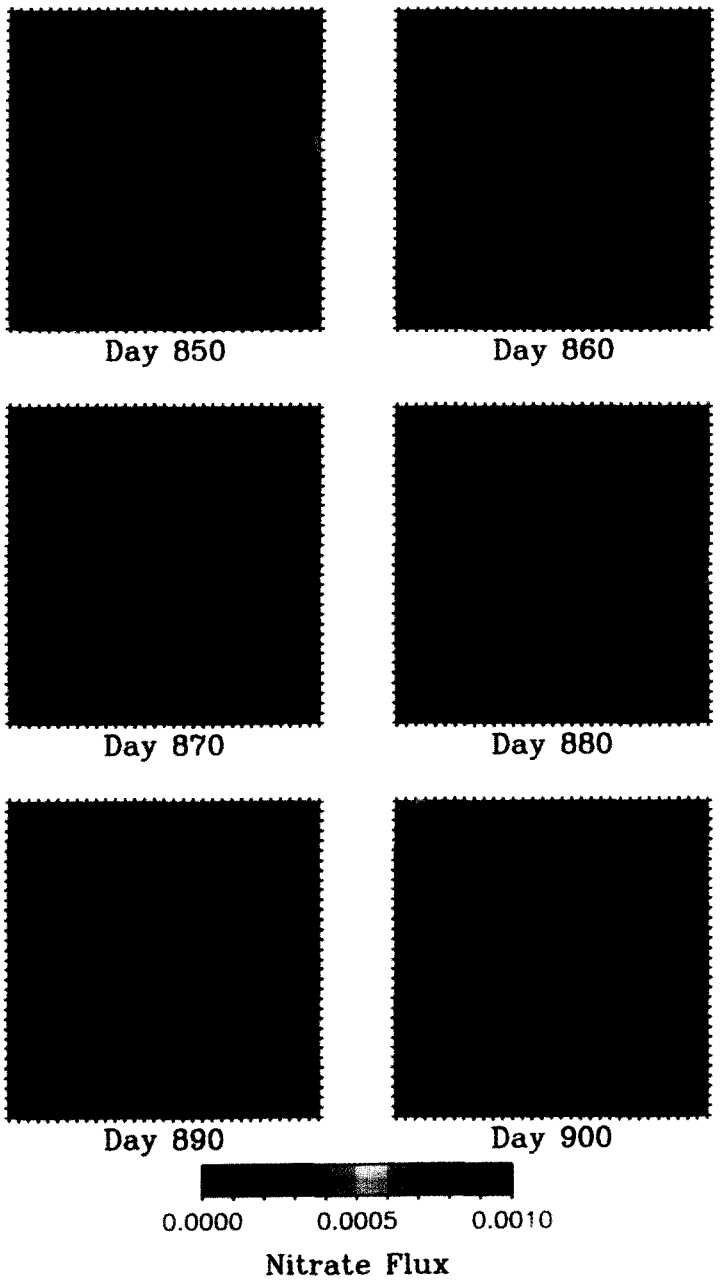

Fig. 7. Time series of simulated nitrate flux into the euphotic zone (mol N m^{-2} day^{-1}) extracted from the interior subdomain during days 850–900. Overlay contours show mixed layer temperature patterns from Fig. 6. Note that the color bar has been truncated at 0.001; peak values actually approach 0.003.

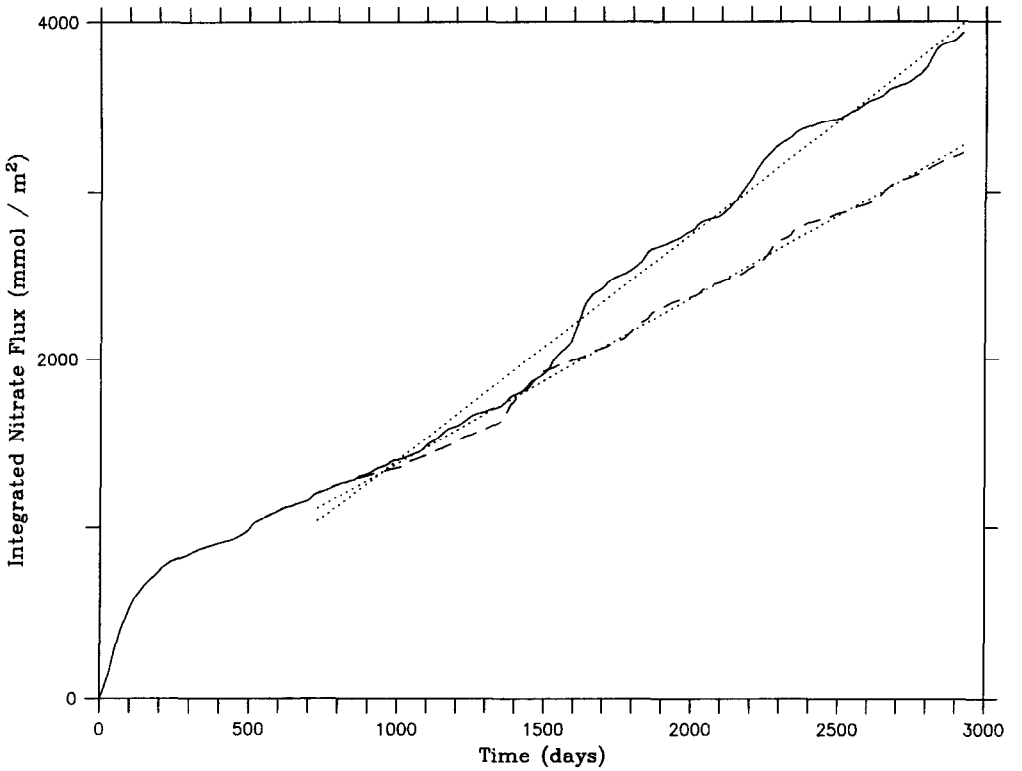

Fig. 8. Time series of integrated nitrate flux spatially averaged over the interior subdomain. The solid and dashed lines correspond to the simulations with and without wind forcing, respectively. Linear least squares fits to both cases are shown for the time periods after the initial adjustment phase.

the euphotic zone by the upwelling inside the cold feature are fixed by the biota, whereas the downwelling of the surface in the warm eddy does not induce any biological response. The asymmetry imposed by the light field thus rectifies vertical displacements of both signs into a net upward transport of nutrients.

The simple kinematics of this eddy upwelling process permit straightforward tabulation of the nutrient flux caused by events of this type using the observed mean summertime nitrate profile. Table 1 lists the integrated nutrient transport induced by eddy events of various magnitudes. Examination of a time series of nutrient flux extracted from the model solution at a single point within the domain (Fig. 10) reveals the presence of events of various magnitudes. The episode that occurs between days 2790 and 2850 is associated with the passage of a developing cyclone directly over the time series point in which the nutrient isopleths from as deep as 200 m have been lifted into the euphotic zone resulting in a net flux of 0.2 mol N m^{-2}. Events such as these are quite common in the simulated fields, and on average only two to three per year need pass directly over a particular point to account for the entire annual budget. Of course, the time series record includes many "near misses," such as that occuring between days 960 and 980, in which only the periphery of an eddy event was sampled. The record also shows evidence of periods (e.g. days 2200–2260) in

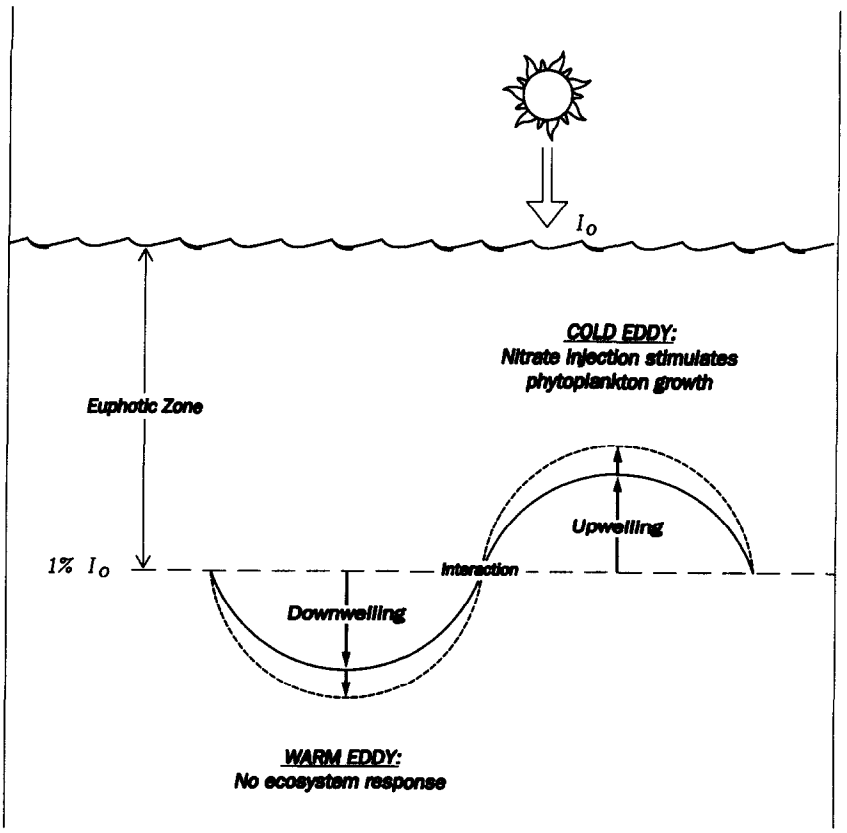

Fig. 9. A schematic representation of the eddy upwelling mechanism. The solid line depicts the vertical deflection of an individual isopycnal caused by the presence of two adjacent eddies of opposite sign. The dashed line indicates how the isopycnal might be subsequently perturbed by interaction of the two eddies.

which large complexes of several interacting cyclonic eddies induce a nutrient flux well in excess of the annual mean in a single event. These complexes occur fairly frequently in the simulated fields, although their formation at any particular point is somewhat rare. Thus, both the spatial and temporal intermittency of this process make it difficult to resolve accurately in traditional time series observations. The nominal 30-day sampling interval used in such operations clearly under-resolves major events, thereby necessitating an extremely long record to construct a meaningful regional budget.

There is some observational evidence that is consistent with the eddy upwelling mechanism. Analysis of CZCS ocean color data from the Sargasso Sea shows significant patchiness in phytoplankton abundance at the eddy length scale (Fig. 11). The spatial structure in phytoplankton biomass is reminiscent of the observed (Voorhis *et al.*, 1976) and simulated patterns of the upper ocean mesoscale physical environment. On several occasions, occupations of the Bermuda time series site for periods of weeks have revealed fluctuations in nutrient inventories and primary productivity on the time scales of several days, which were associated with the passage of different water masses through the sampling

Table 1. *Nitrate flux caused by upward displacement of the mean nitrate profile according to a kinematic representation of the eddy upwelling mechanism*

Depth (m)	$[NO_3]$ (mmol m^{-3})	NO_3 flux/event (mmol m^{-2})	Events/year
70	0.04		
80	0.07	1.1	327.3
90	0.21	3.2	112.5
100	0.31	6.3	57.1
110	0.55	11.8	30.5
120	0.82	20.0	18.0
130	1.12	31.2	11.5
140	1.47	45.9	7.8
150	1.76	63.5	5.7
160	1.96	83.1	4.3
170	2.10	104.1	3.5
180	2.22	126.3	2.8
190	2.35	149.8	2.4
200	2.47	174.5	2.1
210	2.55	200.0	1.8
220	2.64	226.4	1.6
230	2.73	253.7	1.4
240	2.82	281.9	1.3
250	2.91	311.0	1.2
260	3.01	341.1	1.1
270	3.10	372.1	1.0
280	3.20	404.1	0.9
290	3.29	437.0	0.8
300	3.38	470.8	0.7

Nitrate flux per event is calculated by evaluating the $\int_z^{70m}[NO_3]dz$, which represents how much nitrate would be injected into the euphotic zone if water were upwelled from a specified depth horizon. The number of events per year required to supply the annual budget is calculated by dividing the mean eddy driven upwelling estimate from the "no wind" case (0.36 mol N m^{-2} $year^{-1}$) by the nitrate flux per event of specified magnitude.

area (e.g. Malone *et al.*, 1993; Roman *et al.*, 1993; Roman *et al.*, 1995). Recent technological advances have made it possible to deploy automated *in situ* nutrient sensors on moorings (Dickey, pers. commun.). High resolution nitrate time series measured on initial deployments of this new instrument have shown nutrient injections into the euphotic zone of magnitude and duration that are consistent with the eddy upwelling mechanism simulated here.

CONCLUSIONS

The notion that mesoscale eddies could be an important vehicle for nutrient transport in the open ocean has been debated for some time. Quantitative assessment of their impact on annual budgets has proved to be a difficult task because the spatial and temporal intermittency of the phenomena makes a purely observational approach infeasible. However, numerical simulation offers an alternative method for investigation of this issue.

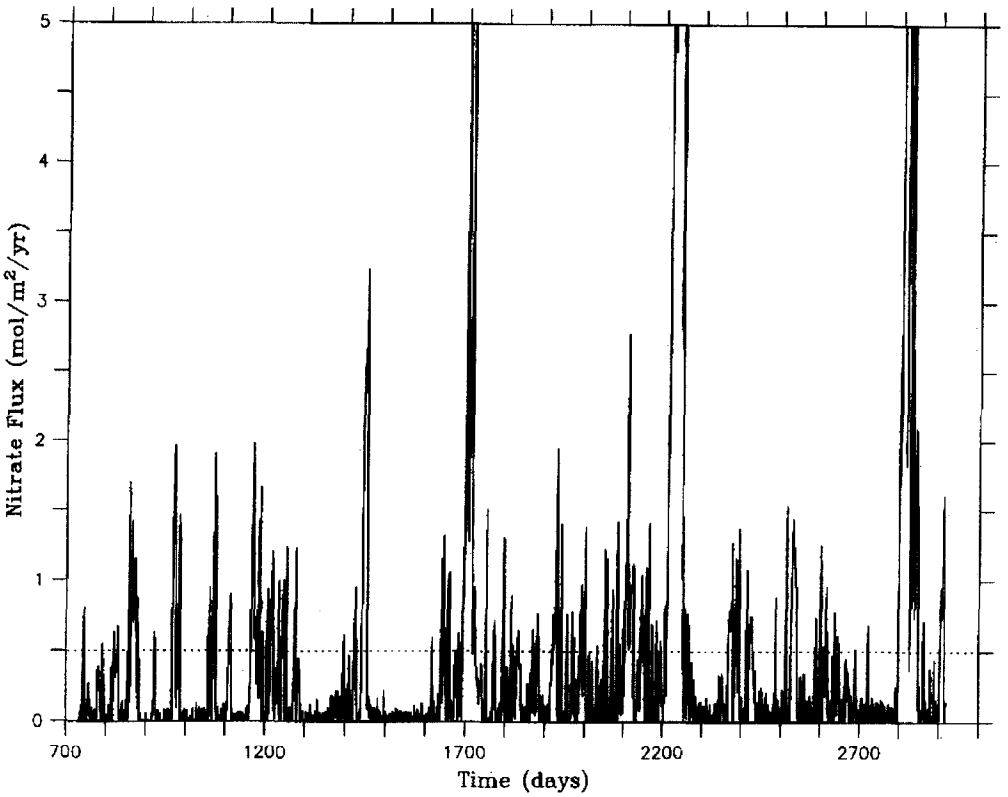

Fig. 10. Time series of simulated nitrate flux extracted from a particular point within the domain. The dashed line indicates the spatially and temporally integrated annual mean flux. Note that values exceeding the maximum ordinate have been truncated.

Implementation of a simple biogeochemical model into a realistic representation of the mid-ocean eddy field provides a framework for diagnosis of the impact of mesoscale dynamical processes on nutrient cycling.

Model calculations suggest that eddies induce a net flux of nitrate on the order of 0.5 mol N m^{-2} year. The bulk of this flux arises from the formation and intensification of cyclonic eddies, while roughly 30% results from upwelling caused by the interaction of mesoscale flows with wind driven surface currents. Although both these mechanisms produce vertical motions of both signs, light imposes a fundamental asymmetry in the system. On the one hand, upwelling imports nutrients into the euphotic zone that are rapidly utilized by phytoplankton. On the other hand, downwelling exports nutrient depleted water out of the illuminated portion of the surface layer, which fails to elicit any ecosystem response. Thus the combination of isotropic vertical motion with biological removal confined to the euphotic zone causes a net upward flux of nutrients. The underlying assumption in this scenario is of course that nutrients are remineralized from sinking organic material on a time scale shorter than the period of vertical displacements caused by the eddies. Because the majority of the nutrient flux is associated with the formation and

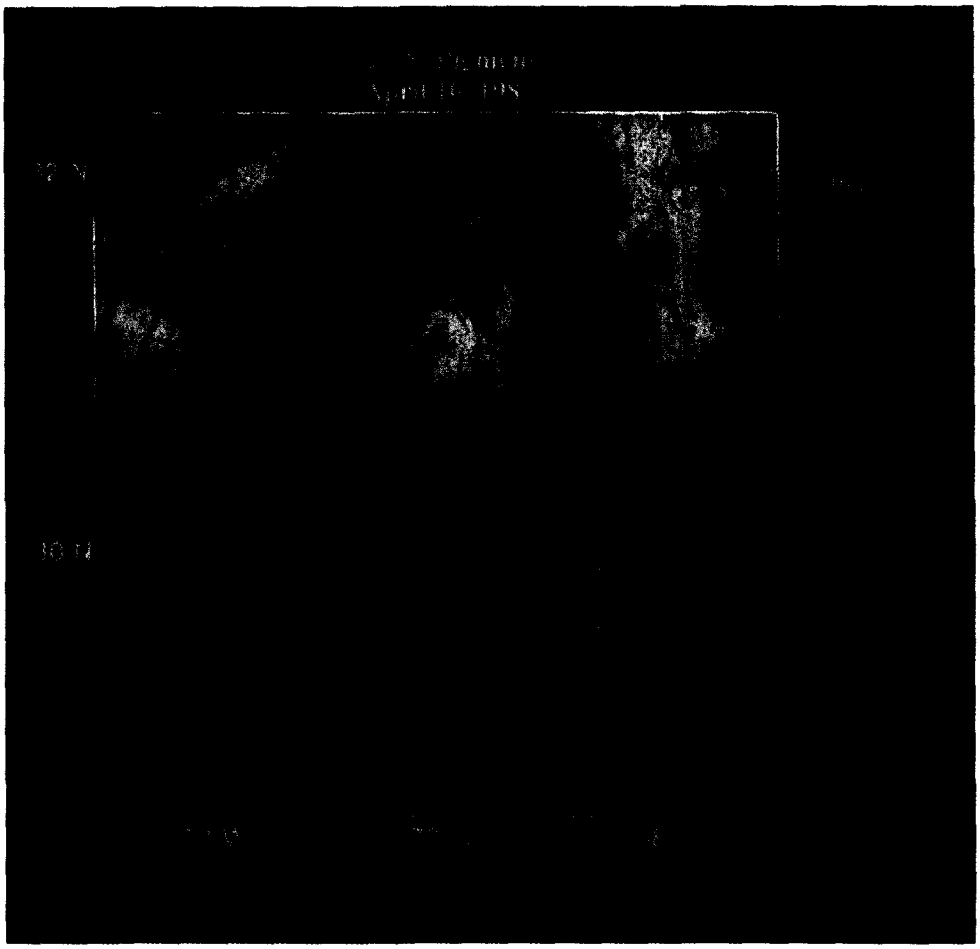

Fig. 11. A CZCS image in the POLYMODE region on 10 April 1981.

intensification of cyclonic eddies, the relevant time scale here is the eddy lifetime. In fact, something like two eddy lifetimes is probably more appropriate because, on average, a water parcel upwelled in the interior of a cyclonic eddy will subsequently be downwelled in an anticyclonic eddy.

From the modeling results presented here it appears that the magnitude of the nutrient flux induced by the cyclonic eddy formation and intensification mechanism is sufficient to balance the levels of new production implied by the various transient tracer observations that are summarized in Table 2. Although the eddy flux clearly falls within the range of uncertainties reported for the tracer inferences, it is on the low side of the range of means from the different methods. However, it is important to point out that while the eddy flux may be the dominant mode of nutrient transport, it is not the only one. Specifically, nitrate mixed into the euphotic zone during wintertime convective mixing does contribute a meaningful portion of the annual budget. Michaels *et al.* (1994) used short-term changes in oxygen and nitrate inventories during the late winter to early spring period of the 1989 BATS time series to estimate that approximately 0.17 mol m^{-2} of new nitrogen was fixed during the bloom period. Clearly this estimate derived from data in a single year must be used with caution in interpreting mean annual budgets. Yet, the sum of the nutrient input due to winter mixing and eddy transport does yield a total flux that is consistent with the tracer observations.

Given that the eddy driven nutrient flux is such a large component of the annual budget, it is somewhat surprising that this mechanism could function largely undetected by the time series at Bermuda. Clearly, one explanation lies in the intermittency of the process. Monthly observations tend to undersample this highly sporadic process. Furthermore, the time scales of biological removal of new nutrient are much quicker (order days) than that of the supply mechanism (order weeks). This dichotomy in time scales makes it very difficult to observe evidence of a nutrient injection directly because it is utilized so quickly. However, oligotrophy does not imply a lack of productivity; ambient nutrient concentration is determined by the balance of supply and removal processes.

While these modeling results are suggestive of a process that could play an important role in biogeochemical cycling in the open ocean, the real challenge will be to observe such events at sea. The fact that their nature poses such problematic sampling requirements necessitates the use of a coupled observational and modeling strategy. With a full complement of remote sensors (altimetry, infra-red imagery, ocean color, and scatterometry), novel *in situ* measurement techniques (such as bio-optical and chemical moorings) and traditional sampling methods, scientists are for the first time equipped to measure a suite of physical,

Table 2. Estimates of new production derived from various transient tracer distributions

Method	New Production (mol N $m^{-2}year^{-1}$)	Reference
Deep sea O_2 utilization	0.7 ± 0.1	Jenkins (1982)
Euphotic zone O_2 accumulation	0.5 ± 0.2	Jenkins and Goldman (1985)
Mixed layer ^3He excess	0.6 ± 0.2	Jenkins (1988a)
Ar and O_2 cycling	0.6 ± 0.2	Spitzer and Jenkins (1989)

biological and chemical variables on space and time scales that were heretofore inaccessible. Assimilation of such data into interdisciplinary models will facilitate the creation of optimal estimates of oceanic fields that are consistent with available observations and dynamically interpolated across data sparse regions. Such space–time continuous representations of the real ocean are ideally suited to the investigation of complex interactive processes such as eddy induced nutrient flux. Moreover, relatively recent progress in ocean prediction and data assimilation has made interdisciplinary ocean forecasting a feasible undertaking. Exploitation of such methodology to guide sampling strategy at sea could significantly improve our ability to observe intermittent processes in the future.

Acknowledgements—During the first part of this work, DJM was supported jointly by the UCAR Postdoctoral Program in Ocean Modeling and the WHOI Postdoctoral Scholarship program. Subsequent funding was provided by NASA's NSCAT Science Team through Jet Propulsion Laboratory contracts 957627 and 960517. ARR was supported by ONR grant N00014-95-1-0371. This work benefited from stimulating discussions with Peter Cornillon, Scott Doney, Joel Goldman, Bill Jenkins, Tony Michaels, Dave Siegel and Jim Yoder. Special thanks to John Ryan for preparing Fig. 11. This is WHOI contribution 9331.

REFERENCES

Angel, M. V. and Fasham, M. J. R. (1983) Eddies and biological processes. In *Eddies in Marine Science*, ed. A. R. Robinson, Chap. 22. Springer, Berlin.

Bretherton, F. P. and Karweit, M. J. (1975) Mid-ocean mesoscale modeling. In *Numerical Models of Ocean Circulation*, pp. 237–249. Ocean Affairs Board, National Research Council, National Academy of Sciences, Washington, D.C.

Carton, J. A. (1986) How predictable are the geostrophic currents in the recirculation zone of the north Atlantic? *Journal of Physical Oceanography*, **17**, 751–762.

Unlinked.

Craig, H. and Hayward, T. (1987) Oxygen supersaturation in the ocean: biological versus physical contributions. *Science*, **235**, 199–202.

Dugdale, R. C. and Goering, J. J. (1967) Uptake of new and regenerated forms of nitrogen in primary productivity. *Limnology & Oceanography*, **12**, 196–206.

Eppley, R. W. and Peterson, B. J. (1979) Particulate organic matter flux and planktonic new production in the deep ocean. *Nature*, **282**, 677–680.

Falkowski, P. G., Ziemann, D., Kolber, Z. and Bienfang, P. K. (1991) Role of eddy pumping in enhancing primary production in the ocean. *Nature*, **352**, 55–58.

Flierl, G. R. and Davis, C. S. (1993) Biological effects of Gulf Stream meandering. *Journal of Marine Research*, **51**, 529–560.

Franks, P. J.S., Wroblewski, J. S. and Flierl, G. R. (1986) Prediction of phytoplankton growth in response to the frictional decay of a warm-core ring. *Journal of Geophysical Research*, **91**, 7603–7610.

Garwood, R. W. (1977) An oceanic mixed layer model capable of simulating cyclic states. *Journal of Physical Oceanography*, **7**, 455–468.

Haidvogel, D. B. (1983) Periodic and regional models. In *Eddies in Marine Science*, ed. A. R. Robinson, pp. 404–437. Springer, Berlin.

Jenkins, W. J. (1982) Oxygen utilization rates in North Atlantic subtropical gyre and primary production in oligotrophic systems. *Nature*, **300**, 246–248.

Jenkins, W. J. (1988) Nitrate flux into the euphotic zone near Bermuda. *Nature*, **331**, 521–523.

Jenkins, W. J. (1988) The use of anthropogenic tritium and helium-3 to study subtropical gyre ventilation and circulation. *Philosophical Transactions — Royal Society of London*, **325**, 43–61.

Jenkins, W. J. and Goldman, J. C. (1985) Seasonal oxygen cycling and primary production in the Sargasso Sea. *Journal of Marine Research*, **43**, 465–491.

Klein, P. and Coste, B. (1984) Effects of wind-stress variability on nutrient transport into the mixed layer. *Deep-Sea Research*, **31**, 21–37.

Lee, D., Niiler, P., Warn-Varnas, A. and Piacsek, S. (1994) Wind-driven secondary circulation in ocean mesoscale. *Journal of Marine Research*, **52**, 371–396.

Leetma, A. and Bunker, A. F. (1978) Updated chart of the mean annual wind stress, convergences in the Ekman layers, and Sverdrup transports in the North Atlantic. *Journal of Marine Research*, **36**, 311–322.

Lewis, M. R., Harrison, W. G., Oakley, N. S., Hebert, D. and Platt, T. (1986) Vertical nitrate fluxes in the oligotrophic ocean. *Science*, **234**, 870–873.

Malone, T. C., Pike, S. E. and Conley, D. J. (1993) Transient variations in phytoplankton productivity at the JGOFS Bermuda time series station. *Deep-Sea Research*, **40**, 903–924.

McGillicuddy, D. J., McCarthy, J. J. and Robinson, A. R. (1995) Coupled physical and biological modeling of the spring bloom in the North Atlantic: (i) Model formulation and one dimensional bloom processes. *Deep-Sea Research I*, **42**, 1313–1357.

McGillicuddy, D. J. and Robinson, A. R. Interaction between the oceanic mesoscale and the surface mixed layer. *Dynamics of Atmospheres & Oceans*, in press.

McGillicuddy, D. J., Robinson, A. R. and McCarthy, J. J. (1995) Coupled physical and biological modeling of the spring bloom in the North Atlantic: (ii) three dimensional bloom and post-bloom effects. *Deep-Sea Research I*, **42**, 1359–1398.

McWilliams, J. C. (1974) MODE mean currents and eddy surface intensification. *MODE Hotline News*, **57**, 1–6.

McWilliams, J. C. (1976) Maps from the Mid Ocean Dynamics Experiment. part ii: Potential vorticity and its conservation. *Journal of Physical Oceanography*, **6**, 828–846.

McWilliams, J. C. and Flierl, G. R. (1976) Optimal quasigeostrophic wave analysis of MODE array data. *Deep-Sea Research*, **23**, 285–300.

Michaels, A. F., Knap, A. H., Dow, R. L., Gundersen, K., Johnson, R. J., Sorenson, J., Close, A., Knauer, G. A., Lohrenz, S. E., Asper, V. A., Tuel, M. and Bidigare, R. (1994) Seasonal patterns of ocean biogeochemistry at the U. S. JGOFS Bermuda Atlantic Time-series Study site. *Deep-Sea Research*, **41**, 1013–1038.

Miller, R. N. and Robinson, A. R. (1984) Dynamical forecast experiments with a baroclinic quasigeostrophic open ocean model. In *Predictability of Fluid Motions*, eds G. Holloway and B. J. West, American Institute of Physics, New York.

Musgrave, D. L., Chou, J. and Jenkins, W. J. (1988) Application of a model of upper ocean physics for studying seasonal cycles of oxygen. *Journal of Geophysical Research*, **93**, 15679–15700.

Niiler, P. P. (1969) On the Ekman divergence in an oceanic jet. *Journal of Geophysical Research*, **74**, 7048–7052.

Onken, R. (1992) Mesoscale upwelling and density finestructure in the seasonal thermocline — a dynamical model. *Journal of Physical Oceanography*, **22**, 1257–1273.

Pinardi, N. and Robinson, A. R. (1987) Dynamics of deep thermocline jets in the POLYMODE region. *Journal of Physical Oceanography*, **17**, 1163–1188.

Platt, T. and Harrison, W. G. (1985) Biogenic fluxes of carbon and oxygen in the ocean. *Nature*, **318**, 55–58.

Richardson, P. L. (1993) A census of eddies observed in North Atlantic SOFAR float data. *Progress in Oceanography*, **31**, 1–50.

Richman, J. G., Wunsch, C. and Hogg, N. G. (1977) Space and time scales of mesoscale motion in the western North Atlantic. *Reviews of Geophysics*, **15**, 385–420.

Rintoul, S. R. and Wunsch, C. (1990) Mass, heat, oxygen and nutrient fluxes and budgets in the North Atlantic Ocean. *Deep-Sea Research*, **38**, 355–377.

Robinson, A. R. and Haidvogel, D. B. (1980) Dynamical forecast experiments with a barotropic ocean model. *Journal of Physical Oceanography*, **10**, 1909–1928.

Robinson, A. R. and Leslie, W. G. (1985) Estimation and prediction of oceanic eddy fields. *Progress in Oceanography*, **14**, 485–510.

Robinson, A. R. and Walstad, L. J. (1987) The Harvard open ocean model: Calibration and application to dynamical process, forecasting, and data assimilation studies. *Applied Numerical Mathematics*, **3**(1-2), 89–131.

Roman, M. R., Caron, D. A., Kremer, P., Lessard, E. J., Madin, L. P., Malone, T. C., Napp, J. M., Peele, E. R. and Youngbluth, M. J. (1995) Spatial and temporal changes in the partitioning of organic carbon in the plankton community of the Sargasso Sea off Bermuda. *Deep-Sea Research I*, **42**, 973–992.

Roman, M. R., Dam, H. G., Gauzens, A. L. and Napp, J. M. (1993) Zooplankton biomass and grazing at the JGOFS Sargasso Sea time series station. *Deep-Sea Research I*, **40**, 883–901.

Sarmiento, J. L., Thiele, G., Key, R. M. and Moore, W. S. (1993) Oxygen and nitrate new production and remineralization in the North Atlantic subtropical gyre. *Journal of Geophysical Research*, **95**, 18303–18315.

Shulenberger, E. and Reid, J. L. (1981) The Pacific shallow oxygen maximum, deep chlorophyll maximum, and primary productivity, reconsidered. *Deep-Sea Research*, **28A**, 901–919.

Spall, M. A. (1989) Regional primitive equation modeling and analysis of the POLYMODE data set. *Dynamics of Atmospheres & Oceans*, **14**, 125–174.

Spitzer, W. S. and Jenkins, W. J. (1989) Rates of vertical mixing, gas exchange and new production: estimates from seasonal gas cycles in the upper ocean near Bermuda. *Journal of Marine Research*, **47**, 169–196.

Strass, V. H. (1992) Chlorophyll patchiness caused by mesoscale upwelling at fronts. *Deep-Sea Research*, **39**, 75–96.

Voorhis, A. D., Schroeder, E. H. and Leetma, A. (1976) Influence of deep mesoscale eddies on sea surface temperature in the North Atlantic subtropical convergence. *Journal of Physical Oceanography*, **6**, 953–961.

Walstad, L. J. and Robinson, A. R. (1990) Hindcasting and forecasting of the POLYMODE data set with the Harvard open ocean model. *Journal of Physical Oceanography*, **20**, 1682–1702.

Walstad, L. J. and Robinson, A. R. (1993) A coupled surface boundary layer -quasigeostrophic model. *Dynamics of Atmospheres & Oceans*, **18**, 151–207.

Woods, J. D. (1988) Mesoscale upwelling and primary production. In *Toward a Theory on Biological-Physical Interactions in the World Ocean*, ed. B. J. Rothschild. D. Reidel, Dordrecht.

APPENDIX

Model description

The physical model consists of a coupled quasigeostrophic and surface boundary layer (QG-SBL) (Walstad and Robinson, 1993) with algorithmic improvements discussed in McGillicuddy (1993) McGillicuddy and Robinson (in press). In the following exposition, equations for the quasigeostrophic interior are nondimensional while those for the surface boundary layer are presented in dimensional form.

The prognostic equation for the vorticity of the interior fluid is

$$\frac{\partial \zeta}{\partial t} + \alpha J(\psi, \zeta) + \beta \psi_x = F_{pqr} \tag{A1}$$

where ψ is the streamfunction and ζ is the dynamic vorticity given by

$$\zeta = \nabla_H^2 \psi + \Gamma^2 (\sigma \psi_z)_z. \tag{A2}$$

The Jacobian J is defined as $J(\psi,\zeta) = \psi_x \zeta_y - \psi_y \zeta_x$, the horizontal Laplacian operator is $\nabla_H^2 = \partial^2/\partial x^2 + \partial^2/\partial y^2$, and F_{pqr} represents a Shapiro filter that is used to parameterize subgridscale dissipation. The nondimensional parameters are

$$\alpha = \frac{V_0 t_0}{D}$$

$$\beta = \beta_0 D t_0$$

$$\Gamma^2 = \frac{f_0^2 D^2}{N_0^2 H^2}$$

where the Coriolis frequency and its meridional gradient are defined as

$$f_0 = 2\Omega \sin \Theta_0$$

$$\beta_0 = \frac{\partial f}{\partial y}$$

and D, H, t_0 and V_0 are characteristic length, depth, time and velocity scales. The stratification is given by

$$\sigma(z) = \frac{N_0^2}{N^2}$$

where

$$N^2 = -\frac{g}{\rho}\frac{\partial \rho}{\partial z}$$

The surface and bottom boundary conditions provide prognostic equations for the top and bottom density

$$\frac{\partial \Gamma^2 \sigma \psi_z}{\partial t} + \alpha J(\psi, \Gamma^2 \sigma \psi_z) = \begin{cases} w^1 & \text{at } z = 0 \\ -\kappa \nabla_H^2 \psi - J(\psi, b) & \text{at } z = -Z \end{cases} \tag{A3}$$

where κ is the bottom friction applied over the topography b. It it through the upper boundary condition that the interior and surface boundary layer models are coupled. The dimensional quasigeostrophic vertical velocity $w^{QG} = V_0 H / f_0 t_0 D \, w^1$ is balanced by the SBL vertical velocity w to maintain the rigid lid approximation at the sea surface

$$w^{QG} + w = 0$$

at

$$z = 0 \tag{A4}$$

The horizontal Ekman velocities are given by

$$\mu = \frac{\partial}{\partial z}\left(\frac{\hat{j} \cdot \vec{\tau}}{\rho}\right)$$

$$v = -\frac{\partial}{\partial z}\left(\frac{\hat{i} \cdot \vec{\tau}}{\rho}\right)$$

with transports

$$\mu_T = \frac{\hat{j} \cdot \vec{\tau}}{\rho_0 f_0}$$

$$v_T = -\frac{\hat{i} \cdot \vec{\tau}}{\rho_0 f_0}$$

The quasigeostrophic contribution to the total vertical velocity at the surface is

$$w^{QG}(z = 0) = \frac{\partial \mu_T}{\partial x} + \frac{\partial v_T}{\partial y} - \frac{1}{f_0}(\mu_T R_x + v_T R_y) - \frac{\beta_0}{f_0} v_T \tag{A5}$$

where R is the relative vorticity at the surface

$$R = \frac{V_0}{D} \nabla_H^2 \psi|_{z=0}$$

Vertical velocities are assumed to vary linearly with depth in this model. As the boundary condition sets the surface value, the vertical derivative of the vertical velocity is used to interpolate the the interior component.

$$\frac{\partial w^{QG}}{\partial z} = -\frac{V_0 \Gamma^2}{f_0 t_0 D} \frac{D}{Dt}(\sigma \psi_z)_z$$

In this model the bottom of the Ekman layer is taken to be at the base of the mixed layer so w vanishes there. Thus ψ is assumed to vary linearly between $-w^{QG}$ and 0 between $z = 0$ and $z = -h$. Equations for the boundary layer buoyancy, temperature and and passive tracer evolution are

$$\rho_t + \alpha(J(\psi^*, \rho) + \mu(\delta_x{}^* + \rho_x) + v(\delta_y{}^* + \rho_y) + (w^{QG} + w)\rho_z) - \frac{w}{\Gamma^2 \sigma} = (M_\rho)_z + \frac{\alpha_T}{c_p} I_z \tag{A6}$$

$$\vartheta_t + \alpha(J(\psi^*, \vartheta) + \mu(\theta_x + \vartheta_x) + v(\theta_y + \vartheta_y) + (w^{QG} + w)\vartheta_z) - w\vartheta_z = (M_\vartheta)_z + \frac{1}{c_p} I_z \tag{A7}$$

$$\phi_t + \alpha(J(\psi^*, \phi) + \mu(\Phi_x + \phi_x) + v(\Phi_y + \phi_y) + (w^{QG} + w)\phi_z) - w\Phi_z + w_\phi(\phi_z + \Phi_z) = (M_\phi)_z + S_\phi \tag{A8}$$

with the quasigeostrophic streamfunction dimensionalized according to

$$\psi^* = V_0 D \psi$$

The density, temperature and tracer perturbations to the mean profile due to interior motions are

$$\delta^* = \frac{\rho_0 f_0 V_0 D}{gH\sigma}(\sigma\psi_z)|_{z=0}$$

$$\theta = \frac{V_0 H\Gamma^2}{f_0 D}\Theta_z(\sigma\psi_z)|_{z=0}$$

$$\phi = \frac{V_0 H\Gamma^2}{f_0 D}\Phi_z(\sigma\psi_z)|_{z=0}$$

where θ and Φ represent the mean temperature and tracer profiles, respectively. Passive tracers can have arbitrary sinking velocities w_ϕ and source terms S_ϕ. The mixing layer depth equation is

$$h_t + uh_x + vh_y + w = e \tag{A9}$$

which must be satisfied at $z = -h$ in the limit approaching from above and below. The entrainment rate e is the flux across the base of the mixing layer. This quantity is derived from the turbulent kinetic energy budget in Garwood's bulk mixed layer model (Garwood, 1977).

Simulations were conducted using a horizontal resolution of 15.625 km. Vertical structure in the QG interior is represented by six levels from the surface to the bottom at 5500 m which are arranged according to the mean stratification. The SBL is nested with the QG grid, spanning the upper 250 m with 10 m resolution. Computational stability requirements of the SBL model in this application demand a time step of approximately 15 min. Subgridscale dissipation is provided by a fourth order Shapiro filter applied once every time step to both QG and SBL components. The QG model is additionally damped by bottom friction [$\kappa = 0.08$ (nondimensional)], while the SBL model includes a uniform turbulent diffusion coefficient of $1.0 \cdot 10^{-5}$ m^2 s^{-1}.